Diamond & Related Materials 156 (2025) 112445

Contents lists available at ScienceDirect

Diamond & Related Materials

journal homepage: www.elsevier.com/locate/diamond

High photosensitization activity of g-C_3N_4 intercalated ZnS nanocrystal for textile dye degradation

M.S. Manojkumar [a,*], B. Sivaprakash [b], D. Tamilselvi [c], R. Rathinam [d]

[a] Department of Biotechnology, Vivekananda College of Engineering for Women, Namakkal 637205, Tamilnadu, India
[b] Department of Chemical Engineering, Annamalai University, Annamalai Nagar 608002, Tamilnadu, India
[c] Rathinam Technical Campus, Coimbatore, Tamilnadu, India
[d] Karpagam College of Engineering, Coimbatore 641032, Tamilnadu, India

ARTICLE INFO

Keywords:
g-C_3N_4/ZnS
MO dye
Z-scheme
Degradation

ABSTRACT

The g-C_3N_4/ZnS nanocomposite material was developed through a wet chemical synthesis process which combined graphitic carbon nitride (g-C_3N_4) with $Zn(NO_3)_2.6H_2O$ to overcome ZnS drawbacks including its large bandgap and fast electron-hole recombination. Scientific analysis of the final materials used X-ray diffraction (XRD), transmission electron microscopy (TEM), UV–visible spectroscopy (UV–Vis), Fourier transform infrared spectroscopy (FTIR), Brunauer–Emmett–Teller (BET) surface area analysis and photoluminescence (PL) spectroscopy for structural, morphological and optical characterization. The efficient construction of a heterojunction between g-C_3N_4 and ZnS elements was enabled by optimizing the g-C_3N_4 concentration which produced better photocurrent response and improved charge separation. Photocatalytic performance of 3 wt% g-C_3N_4/ZnS nanocomposite surpassed all other samples by obtaining 93.0 % MO decomposition using simulated sunlight in 90-minute timeframe. The exceptional efficiency level exceeds numerous previously documented ZnS-based systems which shows that this composite has strong potential for wastewater treatment of organic pollutants. The observed high efficiency in these wastewater treatment systems involves organic pollutants due to the superior performance of the 3 wt% g-C_3N_4/ZnS nanocomposite.

1. Introduction

The rise of semiconductor photocatalysts occurs because they simultaneously reduce environmental pollutions and decrease energy usage [1,2]. TiO_2 stands out as a widely investigated material because of its non-toxic nature combined with low price and durable chemical properties along with remarkable photoreactivity under UV light [3–5]. TiO_2 utilizes a wide band gap that makes it ineffective for visible light applications because it restricts its ability to absorb light [6–9]. Scientists have developed several alternative photocatalytic materials which include metal sulfides, halides, organic polymers, composite oxides and other materials to overcome this constraint. Studies suggest zinc sulfide (ZnS) represents a lot of promise as an alternative photocatalytic material because it belongs to the low-cost II–VI group semiconductors and exists naturally alongside it possessing high electron mobility while remaining environmentally friendly [10–12]. The photocatalysis properties of ZnS are limited by its wide energy band gap of about 3.7 eV [13] and poor visible light absorption along with high rates of photogenerated carrier combination during operation along with photodeterioration after prolonged light usage [14–16]. The development of heterojunction composites using ZnS along with other semiconductors emerged to overcome its known limitations [17]. The photocatalytic performance benefits from these structures because they allow better charge separation and enable broader light absorption [18–20]. Graphitic carbon nitride (g-C_3N_4) emerges as one of the best materials for heterojunction formation because it has excellent thermal/chemical resistance and low toxicity while showing strong visible-light reactions and operating with a 2.7 eV band gap [21–24]. The staggered band alignment between g-C_3N_4 and ZnS allows them to develop a type-II heterojunction [25] that enables efficient photogenerated electron–hole pair separation. The g-C_3N_4 conjugated π-structure improves its ZnS compatibility along with creating uniform ZnS nanoparticle distribution through its high specific surface area [26]. The photocatalytic activity reaches significant improvement when ZnS is anchored onto the g-C_3N_4 framework [27]. The heterojunction interface determines the critical behavior of light absorption while it controls both charge

* Corresponding author.
E-mail address: msmanojkumar1987@gmail.com (M.S. Manojkumar).

https://doi.org/10.1016/j.diamond.2025.112445
Received 11 March 2025; Received in revised form 28 April 2025; Accepted 12 May 2025
Available online 16 May 2025
0925-9635/© 2025 Published by Elsevier B.V.

separation processes and surface redox kinetics [28]. The photocatalytic efficiency becomes subpar when poor interface design occurs. Research indicates that altering the interface leads to better photocarrying performance as well as higher overall efficiency. The study addresses organic pollutant breakdown using photocatalysis but investigates g-C_3N_4-based nanocomposites for antimicrobial functions through ROS production under light exposure.

This research describes the synthesis of g-C_3N_4/ZnS heterojunction composites through an easy aqueous synthesis involving zinc nitrate and thioacetamide and thioglycolic acid combined with g-C_3N_4. Research conducted photochemical experiments on both methyl orange (MO) solution to measure activity levels. The researchers utilized XRD and FT-IR in combination with BET and used TEM, HRTEM along with SAED to examine the composite samples while they employed PL and UV–Vis spectroscopy for optical behavior analysis. The photocatalytic performance enhancement occurs due to the simultaneous benefits of combined g-C_3N_4/ZnS interface functional interaction and efficient charge carrier separation mechanisms.

2. Experiment section

2.1. Materials

The Indian company Sigma Aldrich Co., Ltd. supplied the chemicals: zinc acetate dihydrate (with a concentration of 99.0 %), melamine (with a concentration of 99.5 %). Graphitic carbon nitride, thioglycolic acid, thioacetamide, triethanolamine, ethanol (EtOH, 98 %), P-benzoquinone (BQ), and isopropanol (IPA, 99.7 %) were all provided by Mercury Scientific. Sigma-Aldrich obtained the methyl orange (MO) chemicals. The chemical regents were not subjected to any further experimental purification prior to their use. It was crucial to conduct all experiments with very clean water.

2.2. Preparation of g-C_3N_4 sheets

The synthesis of bulk graphitic carbon nitride (g-C_3N_4) occurred through thermal polymerization of melamine. An entire 12 g portion of melamine received treatment inside an enclosed crucible through a 500 °C furnace process that lasted 4 h under ambient air circulation. The thermal process followed a heating pattern of 5 °C/min to achieve even heat distribution. By using an agate mortar and pestle the yellow product resulted from natural room temperature cooling was ground into a fine bulk g-C_3N_4 powder.

2.3. Intercalation of g-C_3N_4@ZnS nanosheets

A procedure consisted of dissolving 4 mmol zinc nitrate within 80 mL distilled water together with various amounts of prepared g-C_3N_4 powder. The 250 mL duplex round-bottom flask contained the stirred solution where stability was ensured through dropwise addition of 5 mL thioglycolic acid. The mixture was heated to 100 °C. An intrafusion of 20 mL thioacetamide aqueous solution with 8 mmol concentration occurred quickly after addition into the mixture. During the reaction time the mixture was maintained at 100 °C in an oil batch for 6 h. The suspended solution underwent cooling before filtering while using distilled water and ethanol for washing the product to eliminate impurities. The drying process at 80 °C lasted 2 h which led to the formation of the g-C_3N_4/ZnS composite product. The synthesis of pure ZnS as a control sample occurred by following the same method while omitting the introduction of g-C_3N_4.

2.4. Measurement of photocatalytic activity

The photocatalytic degradation tests used a quartz reactor containing a 300 W mercury lamp installed vertically at its center point. The lamp needed a water-cooled jacket to achieve stable reaction temperature control. The artificial sunlight illumination system ran under continuous magnetic stirring to maintain uniformity of the suspension. The catalyst amount remained at 10 mg while its deployment occurred in 60 mL of a 10 mg/L Methyl Orange solution which produced a catalyst-to-solution ratio of 0.167 mg/mL. The photocatalytic mixture experienced dark stirring for 1 h to establish equilibrium mechanisms between pollutant molecules and photocatalytic particles. The solution received exposure to light shortly after dark equilibration time by taking periodic 5 mL aliquots that underwent centrifugation for catalyst separation and later underwent analysis. The analysis of MO solution concentration was performed through UV–Vis spectrophotometry by measuring its maximum absorption peak at ~464 nm. The activity of photocatalysis was studied using phenol as second model pollutant which was initiated at 13 mg/L under the same experimental conditions mentioned for MO.

3. Results and discussions

3.1. UV-DRS analysis

Fig. 1a displays the UV/Vis spectra of the samples that were composed of g-C_3N_4 that were created. The narrower absorption edge of this material results in a lesser intensity compared to that of pure ZnS. There is no doubt that an increase in the concentration of g-C_3N_4 is the driving force behind the expansion of the steep edge absorption threshold and the absorption intensity of g-C_3N_4/ZnS. These are two

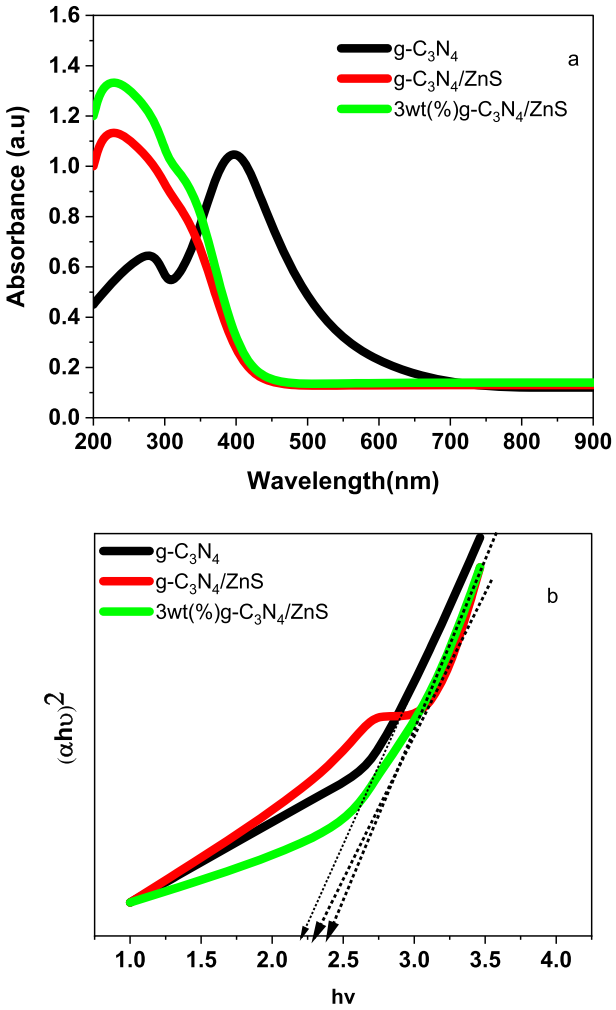


Fig. 1. a) UV-DRS analysis and b) band gap spectra of prepared nanoparticles.

components that significantly contribute to the enhancement of the creation of charge carrier pairs that are generated by photoinduced charge transfer. According to the material's remarkable photocatalytic activity, the absorption edge of the compound that consists of 3 % g-C_3N_4 and zinc sulfide occurs at around 460 nm. This is corroborated by the statement that the substance has. In addition to this, it seems like the colors of the samples are growing more saturated as time passes. Tauc plot method was used in order to ascertain the Eg of g-C_3N_4, g-C_3N_4/ZnS, and 3 wt% g-C_3N_4/ZnS. By using this particular method, it is possible to see the connection that exists between the energy (hσ) and the angular frequency $(\alpha h\sigma)^{n/2}$. A direct band gap is equal to four, whereas an indirect band gap is equal to one. The number n is identical to both of these. There was a rule that was based on the type of the object being assigned, and it was n. According to the data shown in Fig. 1a, the ultraviolet spectrum exhibited the maximum amount of intrinsic absorption for pure ZnS. As can be seen in Fig. 1b, the band gap energy was around 3.69 eV, which is in agreement with the value that was given, which was 3.7 eV. When the wavelength was altered to the visible range, the absorption edges of the ZnS nanoparticles were seen at 360 nm. In addition to this, g-C_3N_4 is capable of detecting visible light with a high degree of clarity, and its band gap of 2.62 eV is lower than the band gap of other made samples of the same material. When g-C_3N_4 is included into g-C_3N_4/ZnS nanocomposites, the absorption edge of these nanocomposites moves to the visible wavelength area at the same time. The peak value at 400 nm rose in a manner that was proportional to the concentration of g-C_3N_4 that was discovered during the experiment. g-C_3N_4/ZnS was found to have a higher Eg value of 2.4 eV in comparison to g-C_3N_4, which was one of the factors that contributed to its decreased absorption up to 440 nm. Upon analysis, it was seen that the presence of g-C_3N_4 nanocomposites led to an increase in the quantity of visible light that ZnS was able to absorb, to a certain extent.

3.2. XRD analysis

Fig. 2 shows the comparison of XRD patterns of g-C_3N_4 and g-C_3N_4/ZnS nanoparticles. XRD patterns of g-C_3N_4/ZnS also shows diffraction peaks matching with the cubic phase structure of zinc sulfide (ZnS) as per standard JCPDS No. 05-0566. In particular, the peaks at 28.5° and 56.4° are assigned to the brightest (002) and (112) planes of ZnS. Furthermore, there is a diffraction peak at 47.5° observed in g-C_3N_4/ZnS composite and which is attributed to (102) plane of ZnO according to JCPDS No. 36-1451. XRD pattern shows the appearance of ZnO peaks which indicates the possible unintended formation of ZnO. This may be

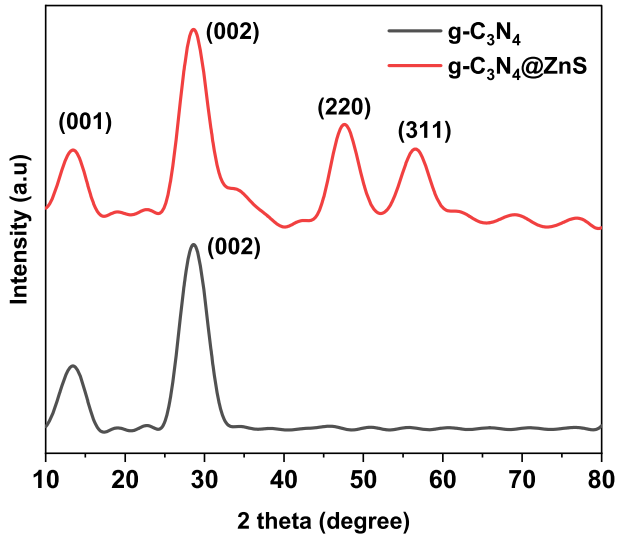


Fig. 2. XRD analysis of prepared nanoparticles.

an indication of partial oxidation of ZnS during its synthesis, most probably the consequence of suboptimal synthesis conditions such as excess oxygen or excessively high temperatures in the calcination. To avoid oxidation of ZnS into ZnO, which is an unwanted by product in the synthesis of composite, these conditions could arise. Partial oxidation of ZnS would be possible under the suboptimal conditions of the reactor, possibly due to suboptimal conditions for ZnS nucleation leading to incomplete oxidation of the species. Nevertheless, the g-C_3N_4 leads to higher crystallinity of ZnS particles, as seen by an increased intensity of the ZnS peaks in the g-C_3N_4/ZnS composite. The peaks intensities of these peaks decrease as concentration of g-C_3N_4 increases, but finally stabilize at 3 wt% g-C_3N_4/ZnS, respectively. It implies that the crystallinity of ZnS particles is also controlled by g-C_3N_4 concentration. In addition, g-C_3N_4 coating of the ZnS particles may cause the agglomeration and growth of ZnS particles, consequently diminishing the degree of crystallization of ZnS in the composite.

3.3. Morphological analysis

An analysis of the 3 wt% g-C_3N_4/ZnS nanocomposite's morphological and structural characteristics took place through transmission electron microscopy (TEM) investigations shown in Fig. 3(a–d). The micrograph in Fig. 3a reveals g-C_3N_4 shows layers of crumpled sheets as its primary structural element. The thin nanosheets extend as an excellent substrate matrix which provides an extensive surface area with various docking points to anchor ZnS nanoparticles. The high magnification image of Fig. 3b shows numerous dark areas representing ZnS nanoparticles that appear clearly throughout the image. The particles spread uniformly across g-C_3N_4 surface because of an effective contact between the materials. Uniform distribution of materials between the components becomes essential because it enables efficient charge carrier separation which leads to better photocatalytic performance. The composite material exists under high magnification in Fig. 3c as it appears through high-resolution TEM (HRTEM). The obtained results display well-defined lattice fringes with an interplanar spacing measurement of 03.1 nm which matches to the (1 1 1) crystal planes of ZnS thereby proving its crystalline structure. The clear appearance of these fringes demonstrates both high crystallinity and excellent quality for the ZnS phase throughout the composite material. The selected area electron diffraction (SAED) analysis of nanocomposite material is presented in Fig. 3d. The sample shows polycrystalline nature because it displays clear concentric rings. XRD and SAED data show that the nanostructure contains crystalline forms of both ZnS and graphitic carbon nitride which specifically match with cubic ZnS and its crystal lattices. The TEM analyses show that the g-C_3N_4/ZnS heterojunction maintains its well-developed structure with homogeneous distribution of nanoparticles and preserves its crystalline characteristics which should enhance its photocatalytic effectiveness.

3.4. Surface characteristics

Studies of nitrogen adsorption and desorption were carried out by the researchers so that they could ascertain the individual surface areas of the samples individually. The nitrogen adsorption-desorption isotherms for g-C_3N_4, g-C_3N_4/ZnS, and a nitrogen sulfide solution with a concentration of 30 % are shown in Fig. 4. According to Fig. 4, the characteristics of pure ZnS combine those of microporous materials at extremely low relative pressure (type I) and mesoporous materials with a type H_3 hysteresis loop at larger relative pressure (type IV). This is shown by the fact that the properties of pure ZnS are hybrid. Isotherms of type IV, which are reported in the literature, demonstrate that g-C_3N_4 has a solid mesoporous structure and demonstrates stepwise adsorption and desorption. As a result, the isotherm of three weight percent g-C_3N_4/ZnS may be deemed the optimal combination of the two chemicals. Zinc sulfide (ZnS) has the potential to attach to g-C_3N_4 and diminish its size as a result of the adsorption sites that g-C_3N_4 may give. The specific surface

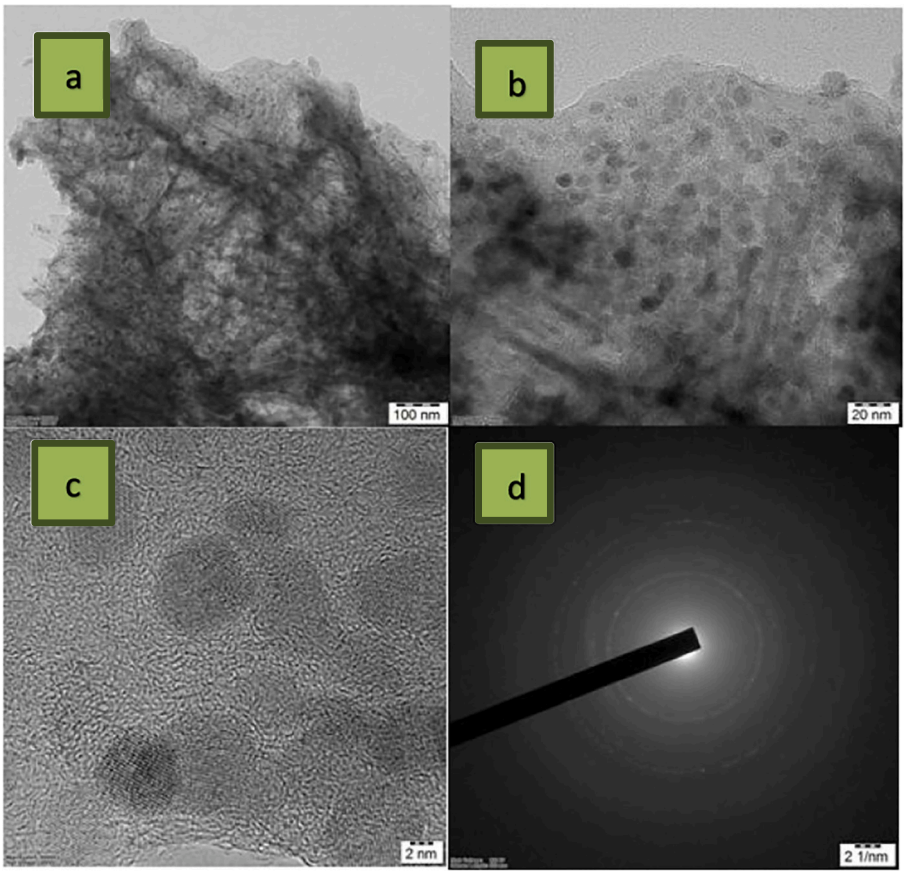


Fig. 3. a) &b) TEM c) HRTEM and d) SAED analysis of 3 wt% g-C_3N_4/ZnS.

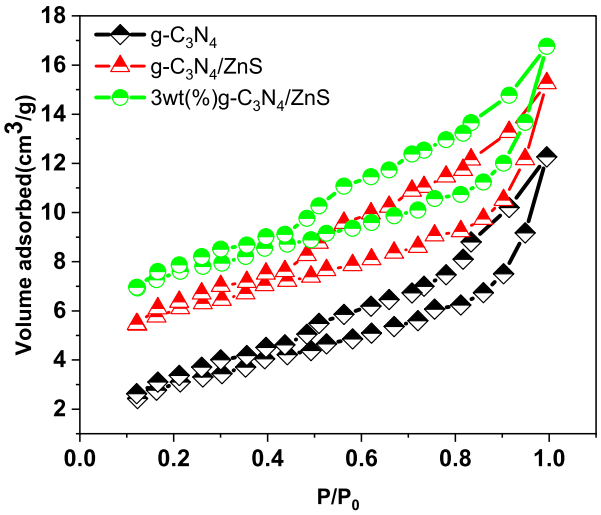


Fig. 4. Surface characteristics of prepared nanoparticles.

area of nanocomposites that include 3 wt% g-C_3N_4/ZnS is 224 square meters per gram, which is much higher than the specific surface area of nanocomposites that only contain g-C_3N_4 (170 square meters per gram). The surface area rise in ZnS-incorporated samples can be explained by several variables despite the common trend of surface area reduction that occurs when incorporating ZnS. The g-C_3N_4 surface had uniform and controlled in-situ ZnS nanoparticle incorporation which avoided agglomeration while maintaining its porous structure. The manufacturing conditions enabled the g-C_3N_4 lattice to partially exfoliate and lead to surface layer increase. The formation of a heterojunction structure between the materials may have created new voids at the interface points which thus increased the total porosity. Parameters during synthesis probably led to a morphology structure which supported greater surface area development. Multiple added factors act together to result in an unexpected BET surface area increase of the composite. When an adsorbent has a bigger surface area, it has the potential to absorb a greater number of dye molecules. Given the statistics, it would seem that the assumption that the outcome corresponds to the deterioration result is supported.

3.5. *Luminescent characterization*

Measurements of photoluminescence (PL) spectra were carried out in order to investigate the optical capabilities of these nanocomposites. The PL spectra of 280 nm excitation are shown in Fig. 5. These spectra are shown for g-C_3N_4, g-C_3N_4/ZnS and a nanocomposite consisting of 3 wt% g-C_3N_4 and ZnS. As a consequence of the enhanced g-C_3N_4 aggregations, the band edge emission of the 3 wt% solution of g-C_3N_4 and ZnS nanoparticles is much greater than that of g-C_3N_4. When surface imperfections are present at low intensities, there is a lower emission from them in comparison to pure ZnS. According to the findings, g-C_3N_4 nanoparticles and ZnS have a strong interaction with one another, and photoinduced electrons easily transfer from ZnS to g-C_3N_4, which results in smaller emission peaks and higher emission levels [29]. The effective electron transport property of g-C_3N_4/ZnS will support an increase in photocatalytic efficiency, in addition to enhancing the separation of electrons and holes.

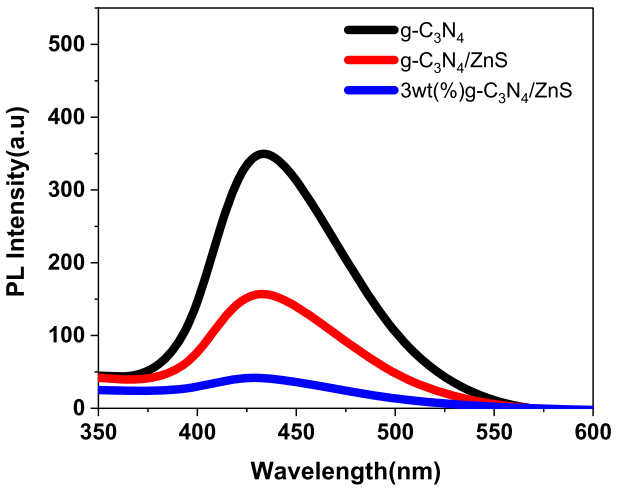


Fig. 5. Luminescent characterization of prepared nanoparticles.

3.6. Photodegrdation performance

A representative sample of 10 wt% g-C_3N_4/ZnS was used to test its adsorption capability with MO and MB in order to pick an appropriate photocatalytic dye. This was done throughout the process of choosing a suitable dye. From what can be observed in Fig. 6a-c, the photocatalyst was able to absorb around 72 % of the MO in only 10 min. On the other hand, the adsorption test demonstrated that a far lower concentration of MO (5 % as opposed to MO) was that which was adsorbed. The aforementioned difference may be attributed to the appearance of a greater number of negative adsorption sites on the surface of the ZnS material. It is easy for MO molecules to adsorb onto the surface of the photocatalyst because of the positive charge that they possess and the electrostatic connections that they have with one another. Due to the presence of a sulfonic acid baseband in MO molecules, it is possible to simplify the process of evaluating the photocatalytic degradation capacity of the g-C_3N_4/ZnS samples. This is accomplished by minimizing the electrostatic interactions that exist between MO and the photocatalyst. The evolution of degradation efficiency for g-C_3N_4 along with g-C_3N_4/ZnS and 3 wt% g-C_3N_4/ZnS under visible light exposure is shown in Fig. 6d. The pure g-C_3N_4 sample achieved only 72 % degradation efficiency during the 90-minute visible light irradiation period. The fast electron-hole pair recombination rate along with the restricted absorption spectrum of pure g-C_3N_4 explains the limited performance. The combination of g-C_3N_4 with ZnS produced a photoactive composite which attained almost 95 % contaminant degradation efficiency. The heterojunction between g-C_3N_4 and ZnS promotes efficient charge separation and allows wider light absorption which results in improved photoreactivity. The heterojunction structure helps photoinduced carriers move while simultaneously minimizing recombination reactions that degrade photocatalytic behavior. The nanocomposite containing 3 wt% g-C_3N_4/ZnS reached 100% degradation efficiency during its reaction period. Maximizing g-C_3N_4 content at the optimized level creates superior photocatalysts because it enhances both light absorption and reaction site and surface area benefits. The particular loading percentage of g-C_3N_4 with ZnS creates enhanced charge carrier dynamics and better pollutant adsorption capabilities by enabling strong interface bonds. Data reveals that adding ZnS to g-C_3N_4 leads to increased photocatalytic degradation performance and 3 wt% proves to be the most powerful sample tested. A set of scavengers was used to learn about the photocatalytic degradation active species during the investigation. A study examining the photocatalytic efficiency of the optimized system under different radical scavenging conditions was performed using IPA, TEOA and BQ. The photocatalytic degradation efficiency faced substantial reduction in the scenarios when BQ and IPA were present in the system. When BQ was added to the reaction mixture it caused an extended drop in degradation efficiency. TEOA showed only a moderate influence on activity because it acts to scavenge holes (h^+) but does not eliminate their participation in the reaction. Without any active scavenger present the degradation exceeded 100 % and confirmed that reactive species work together synergistically in generating the degradation pathway. Superoxide radicals ($^{\bullet}O_2^-$) serve as the main reactive species during photocatalysis with hydroxyl radicals and photogenerated holes presenting secondary effects. Furthermore, photostability is a crucial quality of a photocatalyst, which is well recognized. The efficiency of the 3wt (%) g-C3N4/ZnS has not been significantly reduced after 5 cycles of degradation and regeneration, as seen in Fig. 6f has a very long lifetime. It follows that 3wt (%) 3wt (%) g-C_3N_4/ZnS may effectively lower water pollution levels.

3.7. Kinetic model

A possible representation of the reaction kinetics of MO degradation is the pseudo-first-order Eq. (1), which reads as follows:

$$\ln(C0/Ct) = kt \quad (1)$$

where C_0 represents the pollutant concentration at time 0 and Ct represents the pollutant concentration at time t minutes. The pseudo-first-order reaction has a rate constant of 1 min, which is denoted by the letter k. The kinetics of the corresponding photocatalytic process for MO degradation are shown in Fig. 7. Experimental results showed that the nanocomposite using 3 wt% g-C_3N_4/ZnS displayed the quickest reaction rate while g-C_3N_4/ZnS followed in speed then pure g-C_3N_4. The heterojunction structure leads to better interfacial charge separation and enhanced photocatalytic synergy because of which the efficiency increases.

3.8. Mechanism pathway

A photocatalytic *Z*-scheme mechanism is something that should be investigated in order to get a better understanding of the charge-transfer process that occurs at the interface between g-C_3N_4 and ZnS. This process is activated by visible light. As can be seen in the Fig. 8, ZnS is able to create electron-hole pairs when it is subjected to artificial sunshine. In order to get things started, we need to make it seem as if sunlight is beaming down on zinc sulfide (ZnS) molecules and transport electrons from their highest occupied molecular orbit (HOMO) to their lowest unoccupied molecular orbit (LUMO). In order to facilitate the movement of photogenerated electrons in both directions, the electron mediator must possess the capability to transfer electrons from the LUMO of ZnS to the HOMO of g-C_3N_4. For your information, the amorphous structure of g-C_3N_4 increases the transfer from the conduction band (CB) of ZnS to the valence band (VB) of g-C_3N_4 far more efficient. The role that the electron mediator performs is one that is quite important. Additionally, the electrons that are located in the gC_3N_4 HOMO are transported to the LUMO. It should come as no surprise that the g-C_3N_4 LUMO and the ZnS HOMO are the ones that occupy the electrons that are produced by the photoenergy. To bring this debate to a close, the reducing electrons in g-C_3N_4 have the potential to easily grab the oxygen that has been deposited on the surface. As a result of the quick process that these electrons go through, the production of one component of oxygen occurs. It is possible for organic pollutants to be broken down into smaller molecular bits when the active ions h^+ and O^{2-} are present. Due to the fact that they serve both as mediators and transporters between electrodes, g-C_3N_4 nanosheets are able to improve the photocatalytic activity of the composite and extend the lifespan of its charge carriers [30,31].

4. Conclusion

When it came to the production of g-C_3N_4/ZnS composites at low

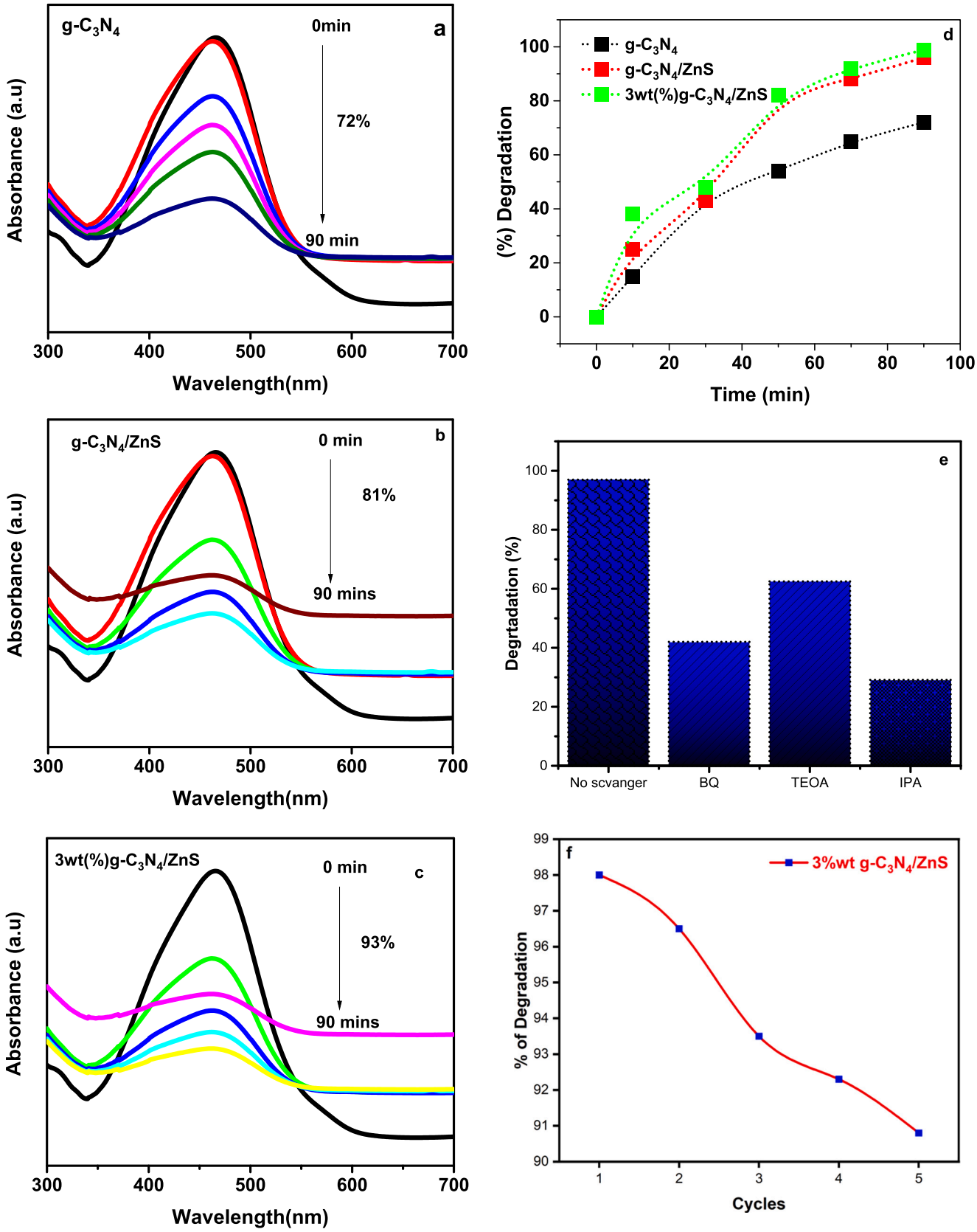


Fig. 6. Photodegrdation using g-C_3N_4 (a), g-C_3N_4/ZnS (b), 3wt(%)g-C_3N_4/ZnS (c), effect of degradation (d), scavenger activity (e) and stability (f).

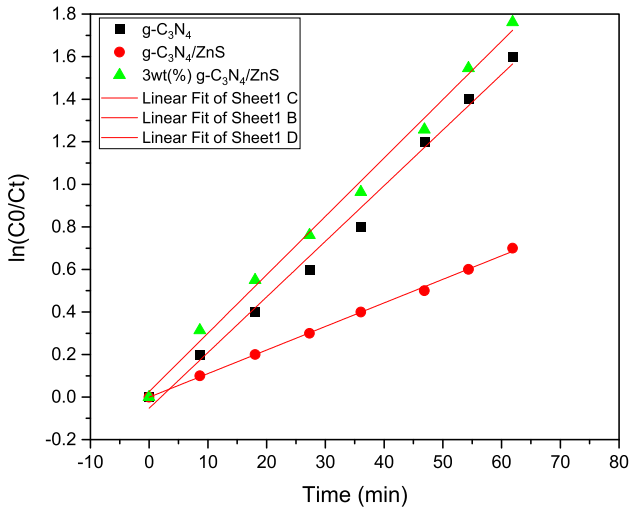


Fig. 7. Kinetic model of prepared nanoparticles.

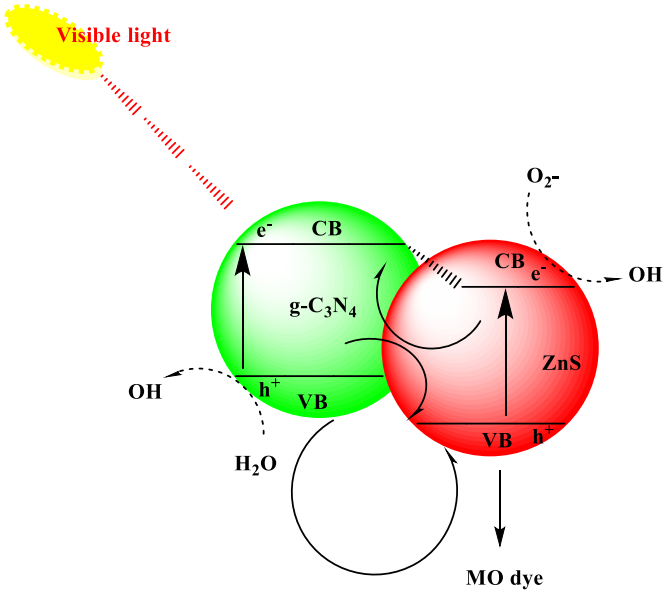


Fig. 8. *Z*-scheme charge transfer mechanism for 3wt(%)g-C_3N_4/ZnS.

temperatures, the wet chemical technique proved to be both effectiveness and efficiency. Additionally, it has been shown that the photocatalytic activity of the g-C_3N_4/ZnS nanocomposite may greatly boost the rate at which MO is degraded. Increasing the surface area of the mixture to 224 m^2g^{-1} and efficiently limiting the recombination of electron-hole pairs in ZnS is accomplished by the incorporation of g-C_3N_4 into the mixture. The material is an excellent photocatalyst due to the fact that it has both of these specific characteristics. This synthesis strategy not only offers a unique material platform for environmental restoration, but it also has the potential to prove to be cost-effective for large-scale operations.

CRediT authorship contribution statement

M.S. Manojkumar: Writing – original draft, Visualization. **B. Sivaprakash:** Visualization, Validation. **D. Tamilselvi:** Writing – original draft, Validation. **R. Rathinam:** Visualization, Validation.

Ethical approval

Not applicable.

Funding

No fundings were received from any research agency and organizations.

Declaration of competing interest

The authors declare that they have no known competing financial interests or personal relationships that could have appeared to influence the work reported in this paper.

Data availability

Data available on reasonable request.

References

[1] M.A. Ahmed, A.A. Mohamed, Recent progress in semiconductor/graphene photocatalysts: synthesis, photocatalytic applications, and challenges, RSC Adv. 13 (1) (2023) 421–439, https://doi.org/10.1039/D2RA07225D.
[2] I. Ahmad, Y. Zou, J. Yan, Y. Liu, S. Shukrullah, M.Y. Naz, N.R. Khalid, Semiconductor photocatalysts: a critical review highlighting the various strategies to boost the photocatalytic performances for diverse applications, Adv. Colloid Interf. Sci. 311 (2023) 102830, https://doi.org/10.1016/j.cis.2022.102830.
[3] F. Zhang, X. Wang, H. Liu, C. Liu, Y. Wan, Y. Long, Z. Cai, Recent advances and applications of semiconductor photocatalytic technology, Appl. Sci. 9 (12) (2019) 2489, https://doi.org/10.3390/app9122489.
[4] F. Opoku, K.K. Govender, C.G.C.E. van Sittert, P.P. Govender, Recent progress in the development of semiconductor-based photocatalyst materials for applications in photocatalytic water splitting and degradation of pollutants, Adv. Sustain. Syst. 1 (7) (2017) 1700006, https://doi.org/10.1002/adsu.201700006.
[5] S. Kavitha, R. Ranjith, N. Jayamani, S. Vignesh, B. Palanivel, R. Djellabi, F. A. Alharthi, Fabrication of visible-light-responsive TiO_2/α-Fe_2O_3-heterostructured composite for rapid photo-oxidation of organic pollutants in water, J. Mater. Sci. Mater. Electron. (2022) 1–14.
[6] S. Kavitha, R. Ranjith, N. Jayamani, Facile construction of novel Ag_2O combined TiO_2 nanocomposites with enhanced dye degradation under visible-light photocatalytic activity, Mater. Technol. 37 (9) (2022) 1205–1219.
[7] K. Thangavelu, R. Rajendran, S. Palanisamy, P. Arumugam, R. Thammasak, Powerful combination of $FeWO_4$/g-C_3N_4 heterostructures for solar light driven photocatalytic degradation of tetracycline and its antibacterial activity, Mater. Today Sustain. 24 (2023) 100562.
[8] R. Rajendran, O. Rojviroon, P. Arumugam, K. Natchimuthu, V. Vasudevan, J. Kannupaiyan, T. Rojviroon, Design and fabrication of g-C_3N_4/Bi_2S_3 heterojunction photocatalysts for efficient organic pollutant degradation and antibacterial activity, J. Alloys Compd. 976 (2024) 173116.
[9] J. Ran, M. Jaroniec, S.Z. Qiao, Cocatalysts in semiconductor-based photocatalytic CO_2 reduction: achievements, challenges, and opportunities, Adv. Mater. 30 (7) (2018) 1704649, https://doi.org/10.1002/adma.201704649.
[10] H. Li, Y. Zhou, W. Tu, J. Ye, Z. Zou, State-of-the-art progress in diverse heterostructured photocatalysts toward promoting photocatalytic performance, Adv. Funct. Mater. 25 (7) (2015) 998–1013, https://doi.org/10.1002/adfm.201401636.
[11] X. Qiu, Y. Zhang, Y. Zhu, C. Long, L. Su, S. Liu, Z. Tang, Applications of nanomaterials in asymmetric photocatalysis: recent progress, challenges, and opportunities, Adv. Mater. 33 (6) (2021) 2001731, https://doi.org/10.1002/adma.202001731.
[12] J. Chen, F. Qiu, W. Xu, S. Cao, H. Zhu, Recent progress in enhancing photocatalytic efficiency of TiO_2-based materials, Appl. Catal. A Gen. 495 (2015) 131–140, https://doi.org/10.1016/j.apcata.2015.02.013.
[13] A. Di Paola, E. García-López, G. Marcì, L. Palmisano, A survey of photocatalytic materials for environmental remediation, J. Hazard. Mater. 211 (2012) 3–29, https://doi.org/10.1016/j.jhazmat.2011.11.050.
[14] S. Algarni, V. Tirth, T. Alqahtani, S. Alshehery, P. Kshirsagar, Contribution of renewable energy sources to the environmental impacts and economic benefits for sustainable development, Sustain Energy Technol Assess 56 (2023) 103098, https://doi.org/10.1016/j.seta.2023.103098.
[15] C. Xia, H. Wang, J.K. Kim, J. Wang, Rational design of metal oxide-based heterostructure for efficient photocatalytic and photoelectrochemical systems, Adv. Funct. Mater. 31 (12) (2021) 2008247, https://doi.org/10.1002/adfm.202008247.
[16] W. Ouyang, F. Teng, J.H. He, X. Fang, Enhancing the photoelectric performance of photodetectors based on metal oxide semiconductors by charge-carrier engineering, Adv. Funct. Mater. 29 (9) (2019) 1807672, https://doi.org/10.1002/adfm.201807672.

[17] R.B. Marcelino, C.C. Amorim, Towards visible-light photocatalysis for environmental applications: band-gap engineering versus photons absorption—a review, Environ. Sci. Pollut. Res. 26 (2019) 4155–4170, https://doi.org/10.1007/s11356-018-3117-5.
[18] Y. Ma, J. Li, J. Cai, L. Zhong, Y. Lang, Q. Ma, Z-scheme g-C3N4/ZnS heterojunction photocatalyst: one-pot synthesis, interfacial structure regulation, and improved photocatalysis activity for bisphenol A, Colloids Surf. A Physicochem. Eng. Asp. 653 (2022) 130027, https://doi.org/10.1016/j.colsurfa.2022.130027.
[19] D.D. Pathak, D.P. Dutta, B.R. Ravuri, A. Ballal, A.C. Joshi, A.K. Tyagi, An insight into the effect of g-C_3N_4 support on the enhanced performance of ZnS nanoparticles as anode material for lithium-ion and sodium-ion batteries, Electrochim. Acta 370 (2021) 137715, https://doi.org/10.1016/j.electacta.2021.137715.
[20] S. Vignesh, H. Kim, Rational construction of efficient ZnS quantum dots-supported g-C_3N_4 with Co_3O_4 heterostructure composite for bifunctional electrocatalytic hydrogen evolution reaction and environmental pollutant degradation, J. Alloys Compd. 942 (2023) 169077, https://doi.org/10.1016/j.jallcom.2023.169077.
[21] X. Zhou, J. Zou, S. Zhang, M. Pan, W. Gong, Preparation and application of g-C_3N_4-ZnS-DNA nanocomposite with enhanced electrocatalytic activity, Chin. J. Catal. 38 (2) (2017) 287–295, https://doi.org/10.1016/S1872-2067(16)62582-2.
[22] M. Faisal, A.A. Ismail, A.A. Ibrahim, H. Bouzid, S.A. Al-Sayari, Highly efficient photocatalyst based on Ce doped ZnO nanorods: controllable synthesis and enhanced photocatalytic activity, Chem. Eng. J. 229 (2013) 225–233, https://doi.org/10.1016/j.cej.2013.06.004.
[23] H.A. Rangkooy, H. Ghaedi, F. Jahani, Removal of xylene vapor pollutant from the air using new hybrid substrates of TiO_2-WO_3 nanoparticles immobilized on the ZSM-5 zeolite under UV radiation at ambient temperature: experimental towards modeling, J. Environ. Chem. Eng. 7 (4) (2019) 103247, https://doi.org/10.1016/j.jece.2019.103247.
[24] S. Garg, M. Yadav, A. Chandra, S. Gahlawat, P.P. Ingole, Z. Pap, K. Hernadi, Plant leaf extracts as photocatalytic activity tailoring agents for BiOCl towards environmental remediation, Ecotoxicol. Environ. Saf. 165 (2018) 357–366, https://doi.org/10.1016/j.ecoenv.2018.09.024.
[25] A. Fernández-Pérez, G. Marban, Titanium dioxide: a heterogeneous catalyst for dark peroxidation superior to iron oxide, J. Environ. Chem. Eng. 8 (5) (2020) 104254, https://doi.org/10.1016/j.jece.2020.104254.
[26] T. Ghosh, K. Ullah, V. Nikam, C.Y. Park, Z.D. Meng, W.C. Oh, The characteristic study and sonocatalytic performance of CdSe–graphene as catalyst in the degradation of azo dyes in aqueous solution under dark conditions, Ultrason. Sonochem. 20 (2) (2013) 768–776, https://doi.org/10.1016/j.ultsonch.2012.09.005.
[27] A.W.M. Ip, J.P. Barford, G. McKay, Reactive black dye adsorption/desorption onto different adsorbents: effect of salt, surface chemistry, pore size and surface area, J. Colloid Interface Sci. 337 (1) (2009) 32–38, https://doi.org/10.1016/j.jcis.2009.05.015.
[28] M. Danish, M. Muneer, Excellent visible-light-driven Ni-ZnS/g-C3N4 photocatalyst for enhanced pollutants degradation performance: insight into the photocatalytic mechanism and adsorption isotherm, Appl. Surf. Sci. 563 (2021) 150262, https://doi.org/10.1016/j.apsusc.2021.150262.
[29] Y. Ren, D. Zeng, W.J. Ong, Interfacial engineering of graphitic carbon nitride (g-C3N4)-based metal sulfide heterojunction photocatalysts for energy conversion: a review, Chin. J. Catal. 40 (3) (2019) 289–319, https://doi.org/10.1016/S1872-2067(19)63293-6.
[30] K. Mahalakshmi, R. Ranjith, P. Thangavelu, M. Priyadharshini, B. Palanivel, M. A. Manthrammel, Mohd Shkir, B. Diravidamani, Augmenting the photocatalytic performance of direct Z-scheme Bi2O3/g-C3N4 nanocomposite, Catalysts 12 (12) (2022) 1544, https://doi.org/10.3390/catal12121544.
[31] N. Akechatree, R. Rajendran, T. Rojviroon, P. Arumugam, V. Vasudevan, S. Sirivithayapakorn, O. Rojviroon, Development of Z-scheme BiVO4/g-C3N4/rGO heterojunction nanocomposite for enhanced photocatalytic degradation and antibacterial activity, Mater. Res. Bull. 181 (2025) 113119.